Communication

The Global Patterns of Interannual and Intraseasonal Mass Variations in the Oceans from GRACE and GRACE Follow-On Records

Damien Delforge [1,2,*], **Olivier de Viron** [1], **Fabien Durand** [3,4] **and Véronique Dehant** [2]

1. Littoral, Environnement et Sociétés, Université de La Rochelle and CNRS (UMR7266), 17000 La Rochelle, France; olivier.de_viron@univ-lr.fr
2. Royal Observatory of Belgium, 1180 Brussels, Belgium; veronique.dehant@oma.be
3. LEGOS (UMR5566), CNRS/CNES/IRD/UPS, 31400 Toulouse, France; fabien.durand@ird.fr
4. Institute of Geosciences, University of Brasilia (UnB), Brasilia 70297-400, Brazil
* Correspondence: damien.delforge@uclouvain.be

Abstract: We decompose the monthly global ocean bottom pressure (OBP) from GRACE(-FO) mass concentration solutions, with trends and seasonal harmonics removed from the signal, to extract 23 significant regional modes of variability. The 23 modes are analyzed and discussed considering sea-level anomalies (SLA), wind stress curl (WSC), and major climate indices. A total of two-thirds of the patterns correspond to extratropical regions and are substantially documented in other global or regional studies. Over the equatorial band, the identified modes are unprecedented, with an amplitude ranging between 0.5 and 1 cm. With smaller amplitude than extratropical patterns, they appear to be less correlated with the local SLA or WSC; yet they present significantly coherent dynamics. The Pacific Ocean modes show significant correlations with the Pacific decadal oscillation (PDO) and El Niño southern oscillation (ENSO).

Keywords: GRACE; ocean; principal component analysis; correlation analysis; sea level anomaly; wind stress curl

1. Introduction

Since 2002, the Gravity Recovery and Climate Experiment (GRACE) and its successor GRACE Follow-On (GRACE-FO) satellite missions allow monthly estimations of ocean mass distributions at the global scale, with a $3° \times 3°$ spatial resolution [1,2]. GRACE products show a sensitivity at the subcentimetric level when expressed in equivalent water height [3,4]. Besides GRACE (-FO), oceanic mass distributions are estimated through a limited set of ocean bottom pressure (OBP) in situ sensors, or from sea-level variations, indirectly, by removing steric effects [4], or using ocean general circulation models (OGCMs). Yet, OGCMs and GRACE (-FO) products have co-evolved along with our understanding of the global ocean. OGCMs offer opportunities for correcting GRACE (-FO) solutions from aliasing errors [5–7]. The physical representativeness of GRACE (-FO) product over oceans was acknowledged early on [3], even more today with recent mass concentration solutions that are better matching with in situ OBP sensors [8–10]. Conversely, empirical analyses of GRACE (-FO) products, or their assimilation in OGCMs, offer the opportunity of improving our understanding and model representation of the global ocean functioning [11–13].

Our study is part of this empirical process of understanding and targets the global detection of regionally consistent spatiotemporal patterns within the GRACE (-FO) data. In the literature, such global studies often consist of global sea-level budgets and comparisons with other models or datasets [14–19]. Besides, except for some studies focusing on interannual or intraseasonal variations [20,21], most of these global ocean studies focus on trends or seasonal cycles given the substantial variance that is attributed to these components alongside anthropic concerns about sea-level rise.

Still, there are reasons to expect relevant signals and processes at interannual and intraseasonal time scales. Regarding processes, the mass distribution in the ocean is governed by the hydrostatic equilibrium, which implies that OBP reflects the mass of the ocean-atmosphere fluid column. The effect of the atmosphere tends to cancel out at timescales longer than a few days [22]. Oceanic barotropic signals are supposed to be prominently related to high frequencies [21,23,24] but were also reported at intraseasonal [25,26] and interannual scales [20]. Besides land-ocean transfers, the ocean circulation, mass, and sea-level variations result from water density gradients or wind-driven Ekman transport [27]. Especially at mid-high latitudes such as in the southern ocean [20,21,28,29], regional-scale sea-level variations mostly correspond to barotropic, i.e., depth-independent, wind-driven mass variations [30]. At lower latitudes, OBP variations potentially have a baroclinic contribution, typically at the subcentimetric level [31]. However, instances of regional-scale barotropic sea-level variability were reported [24–26,31]. Climate dynamics also impact sea level and mass variation no matter the triggered mechanism [32,33]. Patterns of OBP variability are often related to climatic modes, especially the El Niño–southern oscillation (ENSO) in the Pacific [34,35].

Hence, by investigating GRACE (-FO) beyond seasonality and trends, we expect to reveal less understood patterns that would remain otherwise hidden and relate them to the above-mentioned processes that are discussed in regional studies. Our decomposition method for identifying patterns in interannual and intraseasonal GRACE (-FO) signals is based on principal component analysis (PCA), also known as empirical orthogonal functions (EOF) [36]. This method was applied in regional GRACE (-FO) study cases [11,37–39] or globally as a collection of regional EOF [40]. Our approach differs as it is combined with a method to select the significant modes followed by a Varimax rotation [41,42]. As far as the dataset allows, the PCA-Varimax produces regionally concentrated patterns, thus comparable with regional case studies for further insights.

2. Data

2.1. GRACE (-FO) Data

We used JPL GRACE (-FO) RL06v02 mascons solution (https://doi.org/10.5067/TEMSC-3JC62, accessed 5 January 2021) [10,43] because of its fine representation of ocean dynamics. The trend, seasonal harmonics at the yearly and six-month periods, and the 161-days tidal alias resulting from S2 semidiurnal solar tide corrections [44] were subtracted by a least-squares fit. The time-domain covered 175 months from April 2002 to October 2020. Missing time-steps are those initially missing in the data or removed because of an incomplete and asymmetric sub-monthly coverage, as identified from the product metadata (Supplementary Table S1).

From the original $0.5° \times 0.5°$ grid, we sampled 10,255 time-series over ocean area beyond 200 m depth, evenly distributed at the 16,002 summits of an icosahedron. We removed areas that were affected by earthquakes above magnitude 8.8: Sumatra 2004, Chile 2010, and Japan 2011. Unrelated with ocean mass variation, earthquakes introduce sharp ruptures, the coseismic effect, and/or changes of trend, the postseismic effect, in the time-series [45]. Finally, time-series were standardized to have a zero mean and a unit standard deviation.

2.2. Co-Related Datasets: Wind Stress Curl, Sea Level Anomaly, and Climate Indices

The barotropic component of sea-level variability linearly responds to the wind stress curl (WSC) under the assumption of quasi-geostrophic balance [30]. Wind data and sea-level anomaly (SLA) were accessed through the Copernicus Climate Change Service (C3S). Both datasets were monthly averaged and coarsened from the $0.25° \times 0.25°$ to the $0.5° \times 0.5°$ grid of GRACE. Wind stress data are computed from ERA5 10 m zonal U and meridional V wind component [46]. SLA is defined from multi-mission satellite altimetry as the deviation from the mean sea surface height from 1993–2012 [47]. The SLA dataset only covers the latitude range $+/-66$ N°. The SLA and WSC time-series are five

time-steps shorter than the GRACE (-FO) time-series due to the unavailability of the most recent time steps at the time of acquisition.

In addition, 42 climate indices were selected from the NOAA Physical Sciences Laboratory or Climate Prediction Center portals. The entire climate indices list is reported in the Supplementary Materials (Table S2). The main manuscript focuses on a smaller set of important indices being discussed: Arctic oscillation (AO), Antarctic oscillation (AAO), multivariate ENSO Index version 2 (MEIv2), North Atlantic oscillation (NAO), and the Pacific decadal oscillation (PDO). For a consistent comparison, all time-series from the co-related datasets were processed with the same treatment as the GRACE (-FO) data (Section 2.1).

3. Spatiotemporal Pattern Definition

Following Vejmelka et al. (2015) [42], we identified GRACE-(FO) spatiotemporal patterns using rotated principal component analysis (PCA-Varimax) [41]. The Vejmelka et al. (2015)'s approach is a three-step procedure: (1) decomposition of the dataset by regular PCA, (2) selection of significant components, and (3) rotation of the components according to the Varimax criterion. The first step, i.e., PCA, identifies a new orthogonal coordinate system to represent the data. This coordinate system is expressed in eigenvectors and eigenvalues, defining the axes' orientation and importance in terms of captured variance.

Typically, one could keep the first nth axes and the associated components to perform a dimension reduction that preserves most of the variance that is initially found in the dataset (step 2). In practice, the number of coordinate axes or components is regularly set based on heuristic thresholds on the captured variance. Instead, Vejmelka et al. (2015)'s approach [42] proposed an objective basis to define this number by comparing the original PCA decomposition with those that were obtained from random substitutes of the original dataset containing independent time-series. Such random substitutes, known as surrogates, are built to preserve some dynamical traits of the original dataset [48]. In our case, the surrogate models result from autoregressive processes of order p (ARp), with p determined independently for each series to minimize the Bayesian Information Criterion [49], and the coefficient fit on the time-series using the linear state-space model framework [50,51]. Accordingly, the generated surrogate datasets consist of spatially independent time-series that are synthesized using random initial values and the AR coefficients that are obtained at each spatial location. Then, we selected the significant PCA components as those whose corresponding eigenvalues were found above a certain percentile (e.g., 99%) of the distribution of eigenvalues resulting from the surrogate data decomposition.

Finally, following PCA and its dimension reduction, the Varimax rotation (step 3) tends to concentrate the energy on a minimum amount of time-series, i.e., to produce regionally concentrated patterns [41]. In the end, the PCA-Varimax components are associated with a spatial pattern and a time dimension as the original GRACE-(FO) dataset, similarly to the PCA components. However, in contrast with the regular PCA, the Varimax rotation provides temporal patterns that are not necessarily uncorrelated.

4. Results

Figure 1 illustrates the selection of the number of principal components: Figure 1a maps the distribution of the p orders of the surrogate models, while Figure 1b shows the comparison between the GRACE (-FO) PCA eigenvalues and those from the decomposition of 100 surrogate datasets. The results led us to select 23 components (0 to 22), capturing together 72% of the original variance.

Figure 2 displays the resulting 23 Varimax spatial patterns by showing the above-98th percentile filled contour of the load. Since it is a percentile, the contours represent equal areas despite possible variations in the patterns' concentration. For more details, the spatial and temporal patterns are shown individually in the Supplementary Materials (Figures S1 and S2). The patterns' labels are centered on the maximum load location and ordered by decreasing percentages of captured variance in the standardized GRACE

(-FO) dataset (CV_{std} column in Table 1). Providing that the PCA-Varimax is applied on the standardized dataset, CV_{std} gives an estimate of the spatiotemporal importance of the identified dynamics regardless of their physical magnitude. From the CV_{std}'s perspective, the Western Equatorial Pacific Pattern #0 is the most important, while Pattern #22, over the Hudson and Baffin Bay, Labrador Sea, North Atlantic, and Mediterranean Sea, is the least significant.
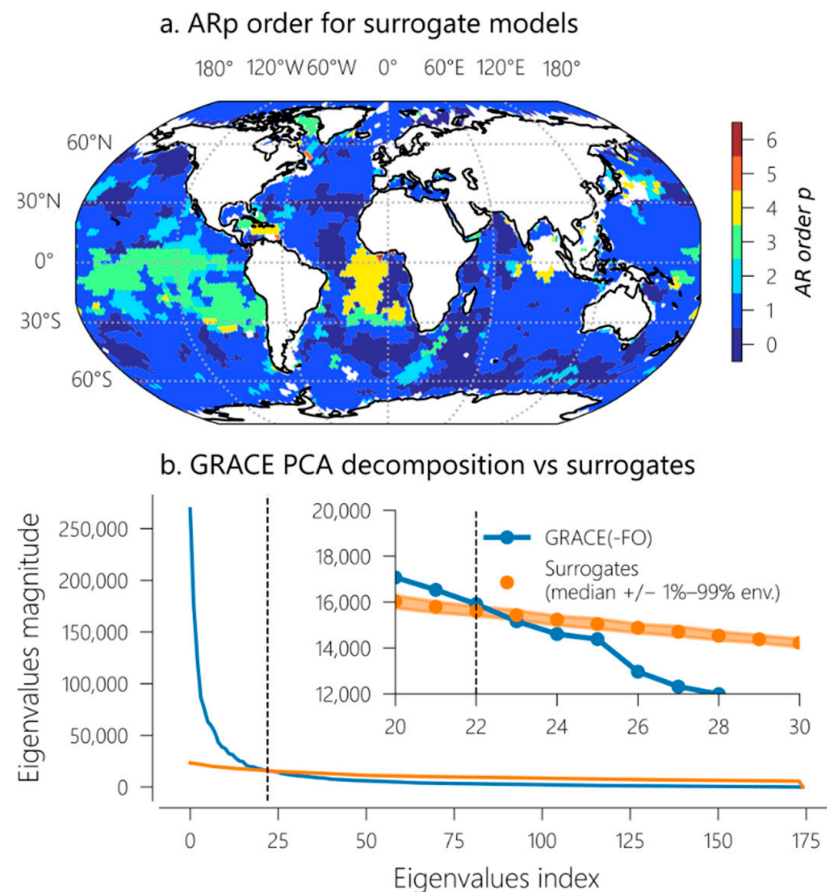

Figure 1. Selection of the 23 PCA components. (**a**) Order of the surrogates model, and (**b**) comparison of the eigenvalues magnitude between the decomposition of GRACE(-FO) and the surrogate dataset.

Table 1 also displays LWE_{cov} reflecting the importance of the patterns in mass variations (cm of liquid water equivalent or LWE). LWE_{cov} is the average covariance between the standardized GRACE (-FO) PCA-Varimax temporal patterns (Figure S2) and the original GRACE (-FO) time-series, without trends and seasonality, over the 98th percentile envelope shown in Figure 2. From that perspective, the Arctic Pattern #12 is the most important, followed by the Australian-Antarctic Pattern #11. Conversely, the intertropical Atlantic Pattern #1 and #9 are the least important in terms of mass deviations, despite their high captured variance in the normalized dataset (CV_{std}).

The last two columns of Table 1, $|\rho(\#, SLA)|$ and $|\rho(\#, WSC)|$, report the absolute values of Pearson's correlation coefficients between the GRACE (-FO) temporal pattern and the respective temporal projection of the SLA and WSC datasets (Section 2.2). They indicate the coherence between the spatiotemporal pattern of mass variations for sea-level dynamics and the surface WSC. Similar to the significance tests on the eigenvalues (Section 3), we tested the 99% significance by confronting the correlation statistic to those that were obtained with 200 ARp surrogates of the GRACE(-FO) PCA-Varimax temporal pattern. In the Supplementary Materials, Figures S3 and S4 show the spatial patterns of correlations for SLA and WSC, while Figures S5 and S6 report the spatial patterns of correlations for zonal (τ_x) and meridional wind stress (τ_y).

Finally, Figure 3 shows the result of the cross-correlation analysis for time lags between −12 and +12 months for the five selected climate indices: Arctic oscillation (AO), Antarctic oscillation (AAO), multivariate ENSO index version 2 (ENSO MEIv2), North Atlantic oscillation (NAO), and Pacific decadal oscillation (PDO). More indices were tested in the Supplementary Materials (Table S2 and Figure S7). Below, Figure 3b shows the auto-correlation of each PCA-Varimax GRACE-(FO) time-series. The results are presented in the form of cross-correlation clocks. In Figure 3a, given the arrow of time, significant dependencies in the left quadrants denote a potential causal effect of the climate indices on the PCA-Varimax GRACE (-FO) patterns. In Figure 3b, dependencies that are confined to 12 o'clock relate to signals that are dominated by high frequencies (e.g., #15 or #19). Conversely, the patterns with more widespread significant dependencies around 12 o'clock instead match with lower frequency signals.

Table 1. Summary statistics and summary correlation statistics for the 23 PCA-Varimax patterns.

#	Lat. °N	LWE_{cov} cm	CV_{std} %	$\|\rho(\#, SLA)\|$ [0,1]	$\|\rho(\#, WSC)\|$ [0,1]
0	−0.13	0.85	6.42	**0.39**	0.06
1	−14.63	0.54	4.84	0.23	0.02
2	−28.13	0.86	4.07	**0.40**	**0.20**
3	24.38	0.81	4.07	**0.37**	0.14
4	15.88	0.77	4.01	0.16	0.16
5	−40.13	1.21	3.95	0.15	**0.57**
6	−24.63	0.73	3.57	**0.36**	0.03
7	28.38	0.79	3.40	0.12	**0.26**
8	−72.63	1.30	3.37	**0.34 ***	**0.55**
9	22.38	0.55	3.36	**0.23**	0.07
10	−13.13	0.64	3.15	0.00	0.14
11	−48.63	2.11	3.11	**0.67**	**0.69**
12	85.38	2.15	3.01	**0.58 ***	**0.49**
13	35.88	0.68	2.88	0.24	**0.35**
14	−34.13	0.92	2.74	0.19	**0.24**
15	36.38	1.58	2.49	**0.40**	**0.61**
16	−49.13	1.85	2.37	**0.73**	**0.38**
17	−57.13	1.71	2.24	**0.71**	**0.33**
18	−36.13	0.69	2.22	0.06	0.15
19	−58.13	1.45	1.89	**0.64**	**0.70**
20	−39.13	0.81	1.81	0.09	0.02
21	48.38	0.76	1.76	0.11	**0.30**
22	35.88	1.00	1.53	**0.42**	**0.26**

Legend: Lat: Latitude of the pattern based on Figure 2 label's position; LWE_{cov}: Average covariance between the standardized GRACE-FO temporal pattern and the original GRACE (-FO) dataset over the 98th percentile envelope shown in Figure 2; CV_{std} : Percentage of the captured variance for the standardized GRACE (-FO) dataset; $\|\rho(\#, SLA)\|$: Absolute Pearson's correlation coefficient between the GRACE (-FO) temporal pattern **#** and the temporal projection of the SLA dataset onto the GRACE (-FO) Varimax coordinate system; $\|\rho(\#, WSC)\|$ **:** Idem for the WSC dataset; In **bold**: significant correlation coefficient ρ from the surrogate testing *****: The values are potentially biased at the pole as the SLA spatial domain is limited to +/−66 N°.
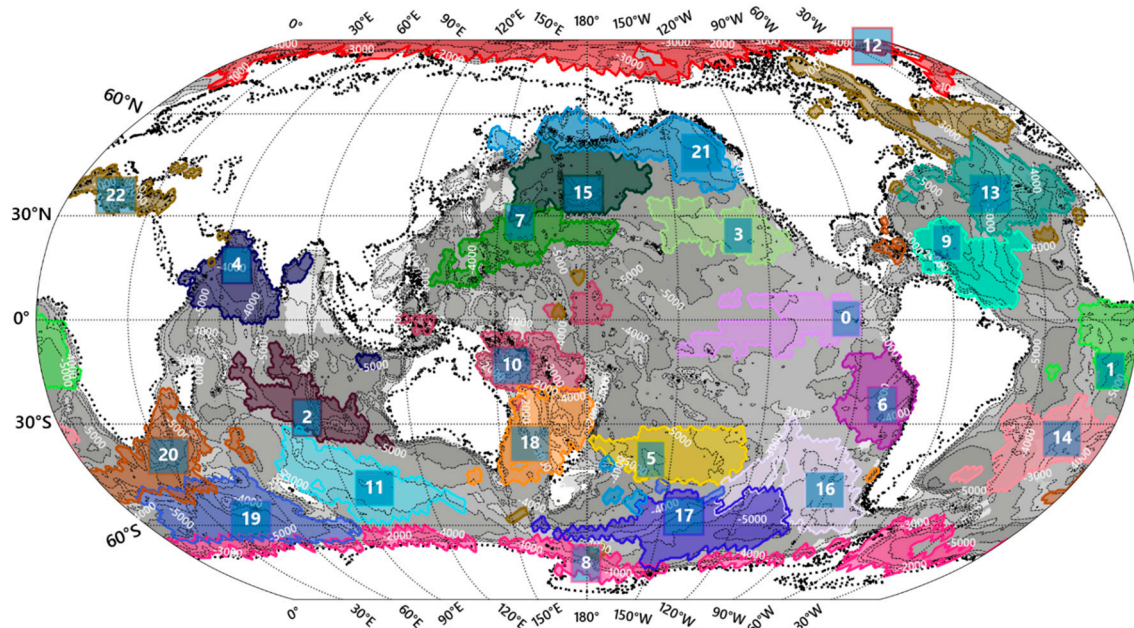
Figure 2. The 23 patterns that were obtained from the Varimax rotation of the PCA coordinate systems. Each pattern is sorted by decreasing captured variance and labeled accordingly from 0 to 22, with the label box located at the Varimax pattern's maximum concentration. The colored contour shows the extent of the area between 98% and the maximum. The gray background contours represent the ocean SRTM15+ bathymetry in meters [52]. White areas represent either land, shallow ocean (>−200 m), or earthquake-impacted areas that were excluded from the analysis. The colormap was generated using colorgorical [53].
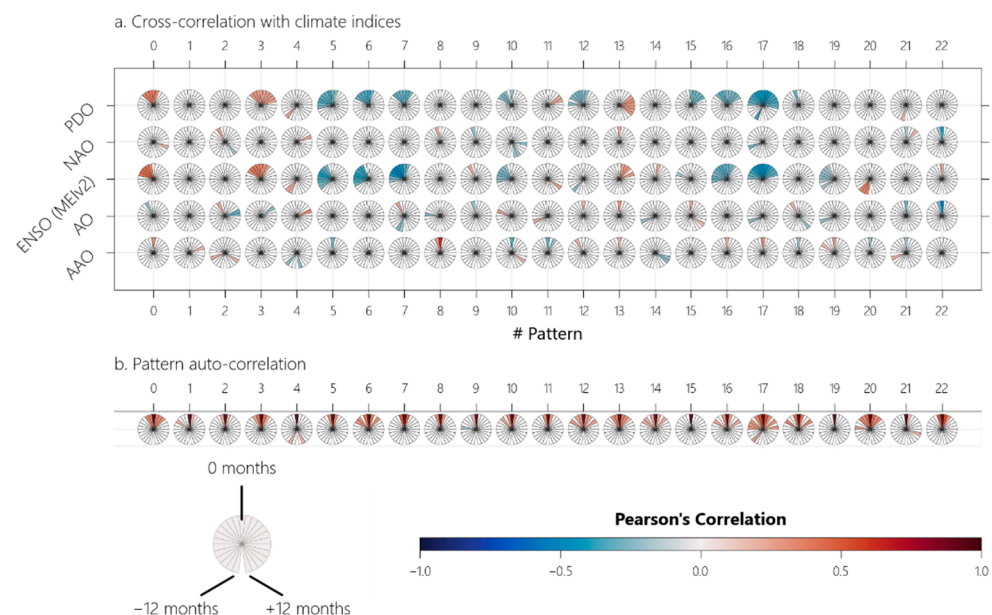
Figure 3. Cross-correlation analysis between the PCA-Varimax GRACE (-FO) patterns and (**a**) the climate indices Arctic oscillation (AO), Antarctic oscillation (AAO), multivariate ENSO Index version 2 (ENSO MEIv2), North Atlantic oscillation (NAO), and Pacific decadal oscillation (PDO); and (**b**) the auto-correlation of the pattern. The results are presented on 25-segments clocks. Only significant dependencies are colored, based on 200 ARp surrogates comparison. 12 o'clock indicates instantaneous correlation. The left quadrants relate to negative lags of the climate indices (**a**) or the pattern (**b**), counterclockwise down to −12 months. The right quadrants contain positive lags clockwise up to +12 months.

5. Discussion

Overall, the significant patterns show spatial consistency, often matching bathymetric contours (Figure 2), or having their limits over bathymetric features in line with the known ability of oceanic slopes to trap barotropic transients [26]. Yet relationships with the SLA and WSC are not systematically significant (Table 1, $|\rho(\#, SLA)|$, $|\rho(\#, WSC)|$), whereas such a relationship is expected from the literature [30]. This implies significant remote forcing of SLA by WSC, as already evidenced in some regions of the world ocean [25,26], and/or a prominent fraction of SLA variability that is baroclinic in nature. In Figure 4, correlations between WSC and the load patterns from Table 1 are plotted against latitude. The linear fit shows an overall poleward increase of correlation in both hemispheres, from insignificant values close to the equator to values above 0.2 at higher latitudes.
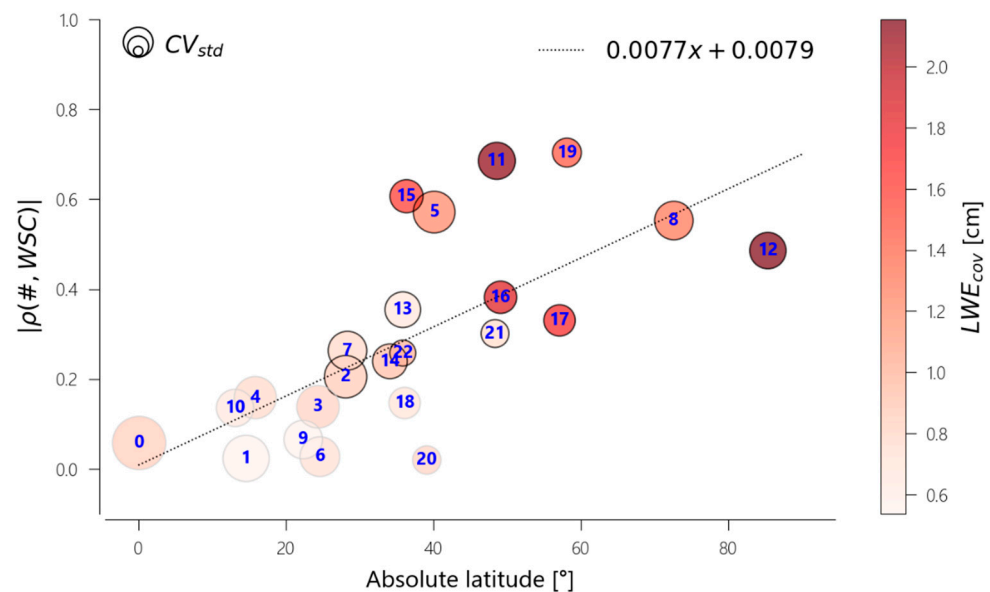
Figure 4. Graphical analysis of the statistics of Table 1. The correlation $|\rho(\#, WSC)|$ between the temporal PCA-Varimax GRACE (-FO) patterns and temporal projections of WSC onto the PCA-Varimax system is reported against the absolute latitude of spatial pattern maximum's concentration (Figure 2). Markers with a black edge have a significant correlation. The markers' size and color, respectively, map to CV_{std} and LWE_{cov}. The pattern index from Figure 2 is labeled in blue.

The mid-latitude Patterns #11, #16, #17, and #19 in the Southern Ocean and #15 in the North Pacific Ocean echo to a highly significant driving by regional winds that is associated with strong mass variations (LWE_{cov}) with a dominant high frequency (Figure 3b). Their load patterns concentrate at medium and high latitudes, as discussed in the literature [20,21,31].

At the North Pole, the high absolute variance Arctic Pattern #12 owes its coherence to the semi-enclosed character of the Arctic Ocean and is wind-driven. It has been the subject of substantial literature [54–56]. In the Northern Atlantic, the Artic pattern is related to #22, as WSC plays an important role in the mass exchange among the Arctic and North Atlantic Ocean [54] (see also Figures S4–S6). This Pattern #22 extends to the semi-enclosed Canadian lakes and the Mediterranean Sea. It was discussed in several studies about its link to NAO (Figure 3) or the Atlantic Meridional Overturning Circulation (AMOC) [57–60]. It shows a smaller consistency (CV_{std}) in Table 1 and Figure 4, probably due to its extensive and fragmented spatial distribution. To the South, Pattern #13 appears to be driven by the wind stress and is statistically related to the AMOC as well as to NAO and AO [61,62] (See Figure 3).

In the North Pacific, Patterns #12 and #21 are connected through the Bering Strait [56,63]. The subpolar Pattern #15 was reported in previous studies focusing on interannual, annual,

or seasonal scales [11,34,64–66]. Accordingly, #15 would be coupled with Pattern #7, which is forced by the ENSO-influenced northern subtropical Pacific gyre (Figure 3). This same Pattern #7 is an area of maxima in terms of dynamic topography that is subject to steep changes in sea level, with the mass component related to the variability of easterlies (Figure S5) and of the north equatorial current over decadal timescales [67–69], in phase with PDO [70] (see Figure 3).

In the southern hemisphere, besides the afore-mentioned highly significant patterns (#11, #16, #17, and #19), the South Pacific Gyre Pattern #5 correlates significantly with SLA and WSC (Table 1 and Figures S4–S6). Together with the Indian Ocean (~#2), this area is exposed to heat uptake and decadal sea-level change where heat transfers are related to Ekman pumping [35,71,72]. It is also associated with transport from the Antarctic bottom water into the Pacific Ocean [35,73]. The South Indian Ocean pattern (~#2) involves both barotropic and baroclinic processes at the annual scale [74]. Other recent studies present further evidence of barotropic processes at intraseasonal timescales over the Indian Ocean [25,26,75]. In a region that is close to our Pattern #14, a sea-level trend that is associated with the Atlantic subtropical gyre has been shown in [76,77]. The Antarctic Pattern #8 is driven by the zonal wind stress (Figure S5i) driving meridional Ekman transport and related to the AAO climate index [78] (see Figure 3). This pattern has been well documented and studied using the GRACE dataset [37,79,80].

Despite their spatially significant dynamical consistency, the remaining ten patterns (#0 to #4, #6, #9, #10, #18, and #20) are not significantly associated with WSC based on our indicator (Table 1, Figure 4), which does not mean that they are uncorrelated with the wind stress, as the correlation is often significant over remote regions that are located outside patterns' boundaries (see Figures S4–S6). They are also less documented in the literature. Still, Pattern #20, corresponding to the eddy-influenced area of the Agulhas current, is discussed in [81], whereas Patterns #10 and #18 correspond to the Coral Sea and the Tasman Sea, both bordered by steep bathymetric features to the east and the north, and known to be influenced by remote WSC from the Maritime Continent at intra-seasonal timescales [25]. The mechanisms of Patterns #0, #3, and #6 remain unclear and may be related to the barotropic response of OBP to remote WSC. They show long memory and are related to ENSO (MEIv2) or PDO (Figure 3a,b). Besides, these patterns may not be physically large enough (LWE_{cov}) to allow identification of significant correlations with WSC and SLA, especially for the weakest ones in the Equatorial Atlantic (#1, #9). Possibly, a part of the OBP response in GRACE(-FO) could be baroclinic but this phenomenon should be marginal (<0.4 cm) and mostly annual [31,74,82,83].

6. Conclusions

We have shown that the spatiotemporal decomposition method, principal component analysis followed by a Varimax rotation (PCA-Varimax), can objectively evidence in a global analysis the GRACE(-FO) patterns that are usually extracted by empirical orthogonal function (EOF) or PCA alone within arbitrary regional bounding boxes. The resulting 23 significant interannual and intraseasonal GRACE (-FO) patterns are spatially coherent and scattered over the global ocean, with mass deviations ranging between 0.54 cm and 2.15 cm. A total of 13 of them significantly relate to wind stress curl and echo to barotropic OBP variations that are documented in the literature. Conversely, the remaining 10 patterns are mainly intertropical and are less documented in the published literature, although our analysis shows that they represent coherent dynamical modes with centimetric mass signatures. Those in the Pacific Ocean are mainly related to the Pacific decadal oscillation (PDO) and El Niño southern oscillation (ENSO). In addition to this empirical analysis, the patterns we have identified would benefit from being studied from a mechanistic perspective, e.g., relying on Ocean Global Circulation Models. In this sense, these particular patterns call for dedicated ocean modeling investigations.

References

1. Landerer, F.W.; Flechtner, F.M.; Save, H.; Webb, F.H.; Bandikova, T.; Bertiger, W.I.; Bettadpur, S.V.; Byun, S.H.; Dahle, C.; Dobslaw, H.; et al. Extending the Global Mass Change Data Record: GRACE Follow-On Instrument and Science Data Performance. *Geophys. Res. Lett.* **2020**, *47*, e2020GL088306. [CrossRef]
2. Tapley, B.D.; Bettadpur, S.; Watkins, M.; Reigber, C. The gravity recovery and climate experiment: Mission overview and early results. *Geophys. Res. Lett.* **2004**, *31*, L09607. [CrossRef]
3. Chambers, D.P. Evaluation of new GRACE time-variable gravity data over the ocean. *Geophys. Res. Lett.* **2006**, *33*, L17603. [CrossRef]
4. Chambers, D.P.; Wahr, J.; Nerem, R.S. Preliminary observations of global ocean mass variations with GRACE. *Geophys. Res. Lett.* **2004**, *31*, L13310. [CrossRef]
5. Dobslaw, H.; Bergmann-Wolf, I.; Dill, R.; Poropat, L.; Thomas, M.; Dahle, C.; Esselborn, S.; König, R.; Flechtner, F. A new high-resolution model of non-tidal atmosphere and ocean mass variability for de-aliasing of satellite gravity observations: AOD1B RL06. *Geophys. J. Int.* **2017**, *211*, 263–269. [CrossRef]
6. Han, S.; Jekeli, C.; Shum, C.K. Time-variable aliasing effects of ocean tides, atmosphere, and continental water mass on monthly mean GRACE gravity field. *J. Geophys. Res. Solid Earth* **2004**, *109*, B04403. [CrossRef]
7. Quinn, K.J.; Ponte, R.M. Estimating high frequency ocean bottom pressure variability. *Geophys. Res. Lett.* **2011**, *38*, L08611. [CrossRef]
8. Piecuch, C.G.; Landerer, F.W.; Ponte, R.M. Tide gauge records reveal improved processing of gravity recovery and climate experiment time-variable mass solutions over the coastal ocean. *Geophys. J. Int.* **2018**, *214*, 1401–1412. [CrossRef]
9. Save, H.; Bettadpur, S.; Tapley, B.D. High-resolution CSR GRACE RL05 mascons. *J. Geophys. Res. Solid Earth* **2016**, *121*, 7547–7569. [CrossRef]

10. Watkins, M.M.; Wiese, D.N.; Yuan, D.; Boening, C.; Landerer, F.W. Improved methods for observing Earth's time variable mass distribution with GRACE using spherical cap mascons. *J. Geophys. Res. Solid Earth* **2015**, *120*, 2648–2671. [CrossRef]

11. Chambers, D.P.; Willis, J.K. Analysis of large-scale ocean bottom pressure variability in the North Pacific. *J. Geophys. Res. Ocean.* **2008**, *113*, C11003. [CrossRef]

12. Fukumori, I.; Wang, O.; Fenty, I.; Forget, G.; Heimbach, P.; Ponte, R.M. *Synopsis of the ECCO Central Production Global Ocean and Sea-Ice State Estimate, Version 4 Release 4*; ECCO Consortium: Washington, DC, USA, 2021.

13. Köhl, A.; Siegismund, F.; Stammer, D. Impact of assimilating bottom pressure anomalies from GRACE on ocean circulation estimates. *J. Geophys. Res. Ocean.* **2012**, *117*, C04032. [CrossRef]

14. Cazenave, A.; Palanisamy, H.; Ablain, M. Contemporary sea level changes from satellite altimetry: What have we learned? What are the new challenges? *Adv. Space Res.* **2018**, *62*, 1639–1653. [CrossRef]

15. Cheng, X.; Ou, N.; Chen, J.; Huang, R.X. On the seasonal variations of ocean bottom pressure in the world oceans. *Geosci. Lett.* **2021**, *8*, 29. [CrossRef]

16. Humphrey, V.; Gudmundsson, L.; Seneviratne, S.I. Assessing Global Water Storage Variability from GRACE: Trends, Seasonal Cycle, Subseasonal Anomalies and Extremes. *Surv. Geophys.* **2016**, *37*, 357–395. [CrossRef]

17. Johnson, G.C.; Chambers, D.P. Ocean bottom pressure seasonal cycles and decadal trends from GRACE Release-05: Ocean circulation implications. *J. Geophys. Res. Ocean.* **2013**, *118*, 4228–4240. [CrossRef]

18. Kanzow, T.; Flechtner, F.; Chave, A.; Schmidt, R.; Schwintzer, P.; Send, U. Seasonal variation of ocean bottom pressure derived from Gravity Recovery and Climate Experiment (GRACE): Local validation and global patterns. *J. Geophys. Res. Ocean.* **2005**, *110*, C09001. [CrossRef]

19. Ponte, R.M.; Quinn, K.J.; Wunsch, C.; Heimbach, P. A comparison of model and GRACE estimates of the large-scale seasonal cycle in ocean bottom pressure. *Geophys. Res. Lett.* **2007**, *34*, L09603. [CrossRef]

20. Piecuch, C.G.; Quinn, K.J.; Ponte, R.M. Satellite-derived interannual ocean bottom pressure variability and its relation to sea level. *Geophys. Res. Lett.* **2013**, *40*, 3106–3110. [CrossRef]

21. Quinn, K.J.; Ponte, R.M. High frequency barotropic ocean variability observed by GRACE and satellite altimetry. *Geophys. Res. Lett.* **2012**, *39*, L07603. [CrossRef]

22. Ponte, R.M. Understanding the relation between wind-and pressure-driven sea level variability. *J. Geophys. Res. Ocean.* **1994**, *99*, 8033–8039. [CrossRef]

23. Gill, A.E.; Niller, P.P. The theory of the seasonal variability in the ocean. *Deep. Sea Res. Oceanogr. Abstr.* **1973**, *20*, 141–177. [CrossRef]

24. Willebrand, J.; Philander, S.G.H.; Pacanowski, R.C. The Oceanic Response to Large-Scale Atmospheric Disturbances. *J. Phys. Oceanogr.* **1980**, *10*, 411–429. [CrossRef]

25. Afroosa, M.; Rohith, B.; Paul, A.; Durand, F.; Bourdallé-Badie, R.; Sreedevi, P.V.; de Viron, O.; Ballu, V.; Shenoi, S.S.C. Madden-Julian oscillation winds excite an intraseasonal see-saw of ocean mass that affects Earth's polar motion. *Commun. Earth Environ.* **2021**, *2*, 139. [CrossRef]

26. Rohith, B.; Paul, A.; Durand, F.; Testut, L.; Prerna, S.; Afroosa, M.; Ramakrishna, S.S.V.S.; Shenoi, S.S.C. Basin-wide sea level coherency in the tropical Indian Ocean driven by Madden–Julian Oscillation. *Nat. Commun.* **2019**, *10*, 1257. [CrossRef] [PubMed]

27. Stammer, D.; Cazenave, A.; Ponte, R.M.; Tamisiea, M.E. Causes for Contemporary Regional Sea Level Changes. *Annu. Rev. Mar. Sci.* **2013**, *5*, 21–46. [CrossRef]

28. Bingham, R.J.; Hughes, C.W. The relationship between sea-level and bottom pressure variability in an eddy permitting ocean model. *Geophys. Res. Lett.* **2008**, *35*, L03602. [CrossRef]

29. Vinogradova, N.T.; Ponte, R.M.; Stammer, D. Relation between sea level and bottom pressure and the vertical dependence of oceanic variability. *Geophys. Res. Lett.* **2007**, *34*, L03608. [CrossRef]

30. Fu, L.-L.; Davidson, R.A. A note on the barotropic response of sea level to time-dependent wind forcing. *J. Geophys. Res.* **1995**, *100*, 24955. [CrossRef]

31. Piecuch, C.G.; Fukumori, I.; Ponte, R.M.; Wang, O. Vertical Structure of Ocean Pressure Variations with Application to Satellite-Gravimetric Observations. *J. Atmos. Ocean. Technol.* **2015**, *32*, 603–613. [CrossRef]

32. Hamlington, B.D.; Piecuch, C.G.; Reager, J.T.; Chandanpurkar, H.; Frederikse, T.; Nerem, R.S.; Fasullo, J.T.; Cheon, S. Origin of interannual variability in global mean sea level. *Proc. Natl. Acad. Sci. USA* **2020**, *117*, 13983–13990. [CrossRef] [PubMed]

33. Han, W.; Meehl, G.A.; Stammer, D.; Hu, A.; Hamlington, B.; Kenigson, J.; Palanisamy, H.; Thompson, P. Spatial Patterns of Sea Level Variability Associated with Natural Internal Climate Modes. In *Integrative Study of the Mean Sea Level and Its Components*; Cazenave, A., Champollion, N., Paul, F., Benveniste, J., Eds.; Space Sciences Series of ISSI; Springer International Publishing: Cham, Switzerland, 2017; pp. 221–254. ISBN 978-3-319-56490-6.

34. Chambers, D.P. ENSO-correlated fluctuations in ocean bottom pressure and wind-stress curl in the North Pacific. *Ocean. Sci.* **2011**, *7*, 685–692. [CrossRef]

35. Volkov, D.L.; Lee, S.; Landerer, F.W.; Lumpkin, R. Decade-long deep-ocean warming detected in the subtropical South Pacific. *Geophys. Res. Lett.* **2017**, *44*, 927–936. [CrossRef] [PubMed]

36. Von Storch, H.; Zwiers, F.W. *Statistical Analysis in Climate Research*; Cambridge University Press: Cambridge, UK, 1999.

37. Liau, J.; Chao, B.F. Variation of Antarctic circumpolar current and its intensification in relation to the southern annular mode detected in the time-variable gravity signals by GRACE satellite. *Earth Planets Space* **2017**, *69*, 93. [CrossRef]

38. Piecuch, C.G.; Fukumori, I.; Ponte, R.M. Intraseasonal Sea Level Variability in the Persian Gulf. *J. Phys. Oceanogr.* **2021**, *51*, 1687–1704. [CrossRef]

39. Wang, Z.; Hamilton, J.; Su, J. Variations in freshwater pathways from the Arctic Ocean into the North Atlantic Ocean. *Prog. Oceanogr.* **2017**, *155*, 54–73. [CrossRef]

40. Marcos, M.; Calafat, F.M.; Llovel, W.; Gomis, D.; Meyssignac, B. Regional distribution of steric and mass contributions to sea level changes. *Glob. Planet. Change* **2011**, *76*, 206–218. [CrossRef]

41. Kaiser, H.F. The varimax criterion for analytic rotation in factor analysis. *Psychometrika* **1958**, *23*, 187–200. [CrossRef]

42. Vejmelka, M.; Pokorná, L.; Hlinka, J.; Hartman, D.; Jajcay, N.; Paluš, M. Non-random correlation structures and dimensionality reduction in multivariate climate data. *Clim Dyn* **2015**, *44*, 2663–2682. [CrossRef]

43. Wiese, D.N.; Landerer, F.W.; Watkins, M.M. Quantifying and reducing leakage errors in the JPL RL05M GRACE mascon solution. *Water Resour. Res.* **2016**, *52*, 7490–7502. [CrossRef]

44. Chen, J.L.; Wilson, C.R.; Seo, K. S2 tide aliasing in GRACE time-variable gravity solutions. *J. Geod.* **2009**, *83*, 679–687. [CrossRef]

45. De Linage, C.; Rivera, L.; Hinderer, J.; Boy, J.-P.; Rogister, Y.; Lambotte, S.; Biancale, R. Separation of coseismic and postseismic gravity changes for the 2004 Sumatra-Andaman earthquake from 4.6 yr of GRACE observations and modelling of the coseismic change by normal-modes summation. *Geophys. J. Int.* **2009**, *176*, 695–714. [CrossRef]

46. Hersbach, H.; Bell, B.; Berrisford, P.; Biavati, G.; Horányi, A.; Muñoz Sabater, J.; Nicolas, J.; Peubey, C.; Radu, R.; Rozum, I.; et al. *ERA5 Monthly Averaged Data on Single Levels from 1979 to Present*; Copernicus Climate Change Service (C3S) Climate Data Store (CDS): Brussels, Belgium, 2019.

47. Taburet, G.; Sanchez-Roman, A.; Ballarotta, M.; Pujol, M.; Legeais, J.; Fournier, F.; Faugere, Y.; Dibarboure, G. DUACS DT2018: 25 years of reprocessed sea level altimetry products. *Ocean. Sci.* **2019**, *15*, 1207–1224. [CrossRef]

48. Schreiber, T.; Schmitz, A. Surrogate time series. *Phys. D Nonlinear Phenom.* **2000**, *142*, 346–382. [CrossRef]

49. Schwarz, G. Estimating the Dimension of a Model. *Ann. Statist.* **1978**, *6*, 461–464. [CrossRef]

50. Durbin, J.; Koopman, S.J. *Time Series Analysis by State Space Methods*, 2nd ed.; Oxford Statistical Science Series; Oxford University Press: Oxford, UK, 2012; ISBN 978-0-19-964117-8.

51. Seabold, S.; Perktold, J. Statsmodels: Econometric and Statistical Modeling with Python. In Proceedings of the 9th Python in Science Conference, Austin, TX, USA, 28 June–3 July 2010; pp. 92–96.

52. Tozer, B.; Sandwell, D.T.; Smith, W.H.F.; Olson, C.; Beale, J.R.; Wessel, P. Global Bathymetry and Topography at 15 Arc Sec: SRTM15+. *Earth Space Sci.* **2019**, *6*, 1847–1864. [CrossRef]

53. Gramazio, C.C.; Laidlaw, D.H.; Schloss, K.B. Colorgorical: Creating discriminable and preferable color palettes for information visualization. *IEEE Trans. Visual. Comput. Graph.* **2017**, *23*, 521–530. [CrossRef]

54. Fukumori, I.; Wang, O.; Llovel, W.; Fenty, I.; Forget, G. A near-uniform fluctuation of ocean bottom pressure and sea level across the deep ocean basins of the Arctic Ocean and the Nordic Seas. *Prog. Oceanogr.* **2015**, *134*, 152–172. [CrossRef]

55. Peralta-Ferriz, C.; Morison, J.H.; Wallace, J.M.; Bonin, J.A.; Zhang, J. Arctic Ocean Circulation Patterns Revealed by GRACE. *J. Clim.* **2014**, *27*, 1445–1468. [CrossRef]

56. Volkov, D.L.; Landerer, F.W. Nonseasonal fluctuations of the Arctic Ocean mass observed by the GRACE satellites. *J. Geophys. Res. Ocean.* **2013**, *118*, 6451–6460. [CrossRef]

57. Fukumori, I.; Menemenlis, D.; Lee, T. A Near-Uniform Basin-Wide Sea Level Fluctuation of the Mediterranean Sea. *J. Phys. Oceanogr.* **2007**, *37*, 338–358. [CrossRef]

58. Piecuch, C.G.; Ponte, R.M. A wind-driven nonseasonal barotropic fluctuation of the Canadian inland seas. *Ocean. Sci.* **2015**, *11*, 175–185. [CrossRef]

59. Tsimplis, M.N.; Calafat, F.M.; Marcos, M.; Jordà, G.; Gomis, D.; Fenoglio-Marc, L.; Struglia, M.V.; Josey, S.A.; Chambers, D.P. The effect of the NAO on sea level and on mass changes in the Mediterranean Sea. *J. Geophys. Res. Ocean.* **2013**, *118*, 944–952. [CrossRef]

60. Volkov, D.L.; Baringer, M.; Smeed, D.; Johns, W.; Landerer, F.W. Teleconnection between the Atlantic Meridional Overturning Circulation and Sea Level in the Mediterranean Sea. *J. Clim.* **2019**, *32*, 935–955. [CrossRef]

61. Landerer, F.W.; Wiese, D.N.; Bentel, K.; Boening, C.; Watkins, M.M. North Atlantic meridional overturning circulation variations from GRACE ocean bottom pressure anomalies. *Geophys. Res. Lett.* **2015**, *42*, 8114–8121. [CrossRef]

62. Piecuch, C.G.; Ponte, R.M. Nonseasonal mass fluctuations in the midlatitude North Atlantic Ocean. *Geophys. Res. Lett.* **2014**, *41*, 4261–4269. [CrossRef]

63. Peralta-Ferriz, C.; Woodgate, R.A. The Dominant Role of the East Siberian Sea in Driving the Oceanic Flow Through the Bering Strait—Conclusions From GRACE Ocean Mass Satellite Data and In Situ Mooring Observations Between 2002 and 2016. *Geophys. Res. Lett.* **2017**, *44*, 11–472. [CrossRef]

64. Bingham, R.J.; Hughes, C.W. Observing seasonal bottom pressure variability in the North Pacific with GRACE. *Geophys. Res. Lett.* **2006**, *33*, L08607. [CrossRef]

65. Song, Y.T.; Qu, T. Multiple Satellite Missions Confirming the Theory of Seasonal Oceanic Variability in the Northern North Pacific. *Mar. Geod.* **2011**, *34*, 477–490. [CrossRef]

66. Song, Y.T.; Zlotnicki, V. Subpolar ocean bottom pressure oscillation and its links to the tropical ENSO. *Int. J. Remote Sens.* **2008**, *29*, 6091–6107. [CrossRef]

67. Moon, J.; Song, Y.T. Sea level and heat content changes in the western North Pacific. *J. Geophys. Res. Ocean.* **2013**, *118*, 2014–2022. [CrossRef]
68. Qiu, B.; Chen, S. Interannual-to-Decadal Variability in the Bifurcation of the North Equatorial Current off the Philippines. *J. Phys. Oceanogr.* **2010**, *40*, 2525–2538. [CrossRef]
69. Timmermann, A.; McGregor, S.; Jin, F. Wind Effects on Past and Future Regional Sea Level Trends in the Southern Indo-Pacific. *J. Clim.* **2010**, *23*, 4429–4437. [CrossRef]
70. Cheng, X.; Li, L.; Du, Y.; Wang, J.; Huang, R. Mass-induced sea level change in the northwestern North Pacific and its contribution to total sea level change. *Geophys. Res. Lett.* **2013**, *40*, 3975–3980. [CrossRef]
71. Llovel, W.; Terray, L. Observed southern upper-ocean warming over 2005–2014 and associated mechanisms. *Environ. Res. Lett.* **2016**, *11*, 124023. [CrossRef]
72. Roemmich, D.; Gilson, J.; Sutton, P.; Zilberman, N. Multidecadal Change of the South Pacific Gyre Circulation. *J. Phys. Oceanogr.* **2016**, *46*, 1871–1883. [CrossRef]
73. Mazloff, M.R.; Boening, C. Rapid variability of Antarctic Bottom Water transport into the Pacific Ocean inferred from GRACE. *Geophys. Res. Lett.* **2016**, *43*, 3822–3829. [CrossRef]
74. Piecuch, C.G.; Ponte, R.M. Annual Cycle in Southern Tropical Indian Ocean Bottom Pressure. *J. Phys. Oceanogr.* **2014**, *44*, 1605–1613. [CrossRef]
75. Manche, S.S.; Nayak, R.K.; Mohanty, P.C.; Shesasai, M.V.R.; Dadhwal, V.K. Assessment of mass-induced sea level variability in the Tropical Indian Ocean based on GRACE and altimeter observations. *J. Geod.* **2021**, *95*, 19. [CrossRef]
76. Drouin, K.L.; Lozier, M.S.; Johns, W.E. Variability and Trends of the South Atlantic Subtropical Gyre. *J. Geophys. Res. Ocean.* **2021**, *126*, e2020JC016405. [CrossRef]
77. Ruiz-Etcheverry, L.A.; Saraceno, M. Sea Level Trend and Fronts in the South Atlantic Ocean. *Geosciences* **2020**, *10*, 218. [CrossRef]
78. Ponte, R.M.; Quinn, K.J. Bottom pressure changes around Antarctica and wind-driven meridional flows. *Geophys. Res. Lett.* **2009**, *36*, L13604. [CrossRef]
79. Feng, G.; Jin, S.; Reales, J.M.S. Antarctic circumpolar current from satellite gravimetric models ITG-GRACE2010, GOCE-TIM3 and satellite altimetry. *J. Geodyn.* **2013**, *72*, 72–80. [CrossRef]
80. Ponte, R.M.; Piecuch, C.G. Interannual Bottom Pressure Signals in the Australian–Antarctic and Bellingshausen Basins. *J. Phys. Oceanogr.* **2014**, *44*, 1456–1465. [CrossRef]
81. Kuhlmann, J.; Dobslaw, H.; Petrick, C.; Thomas, M. Ocean bottom pressure signals around Southern Africa from in situ measurements, satellite data, and modeling. *J. Geophys. Res. Ocean.* **2013**, *118*, 4889–4898. [CrossRef]
82. Piecuch, C.G. Dynamics of satellite-derived interannual ocean bottom pressure variability in the western tropical North Pacific. *J. Geophys. Res. Ocean.* **2013**, *118*, 5117–5128. [CrossRef]
83. Piecuch, C.G. Bottom-pressure signature of annual baroclinic Rossby waves in the northeast tropical Pacific Ocean. *J. Geophys. Res. Ocean.* **2015**, *120*, 2449–2459. [CrossRef]
84. Pedregosa, F.; Varoquaux, G.; Gramfort, A.; Michel, V.; Thirion, B.; Grisel, O.; Blondel, M.; Prettenhofer, P.; Weiss, R.; Dubourg, V.; et al. Scikit-learn: Machine Learning in Python. *J. Mach. Learn. Res.* **2011**, *12*, 2825–2830.